Selected Area Deposition of PtC_x Nanostructures: Implications for functional coatings of 3D Nanoarchitectures

John Lasseter,[1,2], Philip D. Rack[1], Steven J. Randolph[2,]*

1. Department of Materials Science and Engineering, University of Tennessee, Knoxville, Tennessee 37996, United States

2. Center for Nanophase Materials Sciences, Oak Ridge National Laboratory, Oak Ridge, Tennessee 37830, United States

[*]Corresponding author email: randolphsj@ornl.gov

Abstract

We report that selected area deposition of 3D nanostructures is induced via a pyrolytic laser chemical vapor deposition (CVD) process where the selected area heating results from the unique photothermal transport regime that is intrinsic to 3D nanostructure. PtC_x composite nanostructures were deposited by focused electron beam induced deposition (FEBID) and used as the 3D templates. Subsequent simultaneous localized delivery of an organometallic PtC_x

precursor and pulsed 915 nm laser irradiation to the pre-defined nanostructures results in selected area deposition on the FEBID features. Results indicate the ability to initiate the process on sub-diffraction-limit nanoscale features. To elucidate the mechanisms that are operative in the selected area deposition, we analyze the effects of laser repetition rate, power, and pulse duration. Thermal simulations corroborate that the pseudo-1D thermal transport of the nanostructure geometry coupled with the optical and thermal properties of the nanostructure govern the CVD reaction. The results demonstrated here suggest that controlling the thermal transport in nanomaterial architectures could be a useful means to spatially control localized photothermally stimulated chemical reactions and induce selected area reaction.

Introduction

Additive manufacturing and direct write processes have experienced significant growth in the past decade where new materials, techniques, and applications have all emerged. Various size scales have been explored historically but recent pushes have extended three dimensional additive manufacturing towards the micro and nanoscale[1,2]. While several techniques like direct-ink writing[3,4], multi-photon lithography[5,6], electrohydrodynamic printing[7], dip-pen lithography[8], laser induced[9–12] and other methods[13] in principle work in the sub-micron regime, focused electron and ion beam induced deposition (FEBID/FIBID) is likely the most developed technique for synthesizing complex architectures in three dimensions. Several applications have been demonstrated including nanomechanical resonating sensors[14,15], advanced scanning probe tips[16], chiral plasmonics[17], plasmonic split ring resonators[18], and magnetic architectures[19].

In FEBID a focused electron beam is used to decompose precursor molecules that adsorb onto the substrate resulting in the condensation of by-products and the formation of a nanoscale deposit. While accurate control through detailed modeling, simulations[20–25] and 3D computer

aided design infrastructure[26–28] have all been realized for FEBID, challenges remain in this technique. Likely the biggest obstacle for wider scale adoption is the resultant, material quality due to residual carbon incorporation from organometallic precursor fragments[29]. Various precursors have been explored which result in different functionality and purity (see Barth *et al.*[30] for a review of precursors). Trimethyl(methylcyclopentadienyl)platinum ($MeCpPtMe_3$) is the most common precursor and depending on the dose, beam energy, and residual water in the chamber the resultant PtC_x deposit varies from $\sim 5<x<8$[31]. Various metal carbonyls have been explored and the optimum metal content varies: $Cr(CO)_6$ – 20-40 at.% [30], $Mo(CO)_6$ – 8-20 at.% [32,33], $W(CO)_6$ – 37-58at.% [34–36], $Fe(CO)_5$ – 80-95 at.% [37–39], $Fe_2(CO)_9$ – 80-93at.% [40,41], $Co_2(CO)_8$ – 73-100at.% [35,40,42–44] and $Ni(CO)_4$ – 95at.%[45]. Additionally, several groups have explored subsequent coating processes[18], post-electron beam induced curing[29,46–50], co-deposition with purification gases[51,52], beam-induced post-purification with oxidizing[53–57] and reducing[58] precursors, post-deposition annealing[29,54,59–61], and synchronized pulsed laser FEBID[62,63] all aimed at improving material properties without sacrificing the nanoscale 3D direct-write attributes that make the process attractive.

Thus, while FEBID/FIBID are excellent for nanoscale dimensional control, the poor materials quality makes subsequent deposition techniques an important area to study. It is well known the spatial confinement in FEBID nanostructures can result in pseudo 1D heat transport, which results in nanostructure heating that alters the precursor adsorption and decomposition kinetics/thermodynamics[64–67]. PtC_x nanostructures grown via FEBID are used as templates for subsequent selected area laser deposition. For convenience we use the same precursor (trimethyl (methylcyclopentadienyl) platinum ($MeCpPtMe_3$)) as both the FEBID precursor as well as the precursor for the subsequent selected area laser deposition. As we will show, while the ~ 100 μm

diameter focused laser spot irradiates both the underlying substrate and the FEBID nanostructures, the combined optical and thermal properties of the nanoscale FEBID architectures induce selected area photothermal nanostructure heating that may exceed the thermal decomposition threshold of precursor molecules while the underlying substrate is well below the threshold. While we employ FEBID-synthesized architectures for the selected area photothermal chemical vapor deposition (CVD), the strong geometric contribution to thermal transport at the nanoscale implies applicability to other 3D nanofabrication techniques described above. Generally, the phenomenon should be compatible with any nanostructure of proper optical, thermal, and geometric characteristics. Because FEBID deposits using most organometallic precursors result in high carbon content, they have limited as-deposited functionality; thus, the laser CVD process can be used to subsequently selectively coat the 3d architectures with materials containing the desired functionality. Future plans include magnetic coatings with $Co_2(CO)_8$) precursor, and plasmonic coatings derived from dimethyl gold acetylacetonate.

Results and Discussion

Our initial experiments were designed to assess the feasibility of photothermally driving a CVD process that selectively deposits on FEBID 3D nanostructures. Figure 1a illustrates schematically the process where initially a series of nanopillars were grown to various heights via the standard FEBID process using the $MeCpPtMe_3$ precursor, which nominally produces deposits of PtC_x where $5 < x < 10$. Figure 1b illustrates that when the pseudo 1D nanopillars are subsequently exposed to focused, pulsed laser irradiation simultaneously with $MeCpPt^{IV}Me_3$ precursor – the pulsed laser photothermally heats the FEBID nanopillars and induces thermal

decomposition of the precursor. Since the photothermal CVD is driven largely by the characteristic photothermal response of the nanostructure, the deposition can be accomplished on a variety of substrates with only small changes in the growth (see Supporting information S1). Thermal modeling shows significant shifts in the substrate thermal conductivity only modestly shifts the peak temperature.

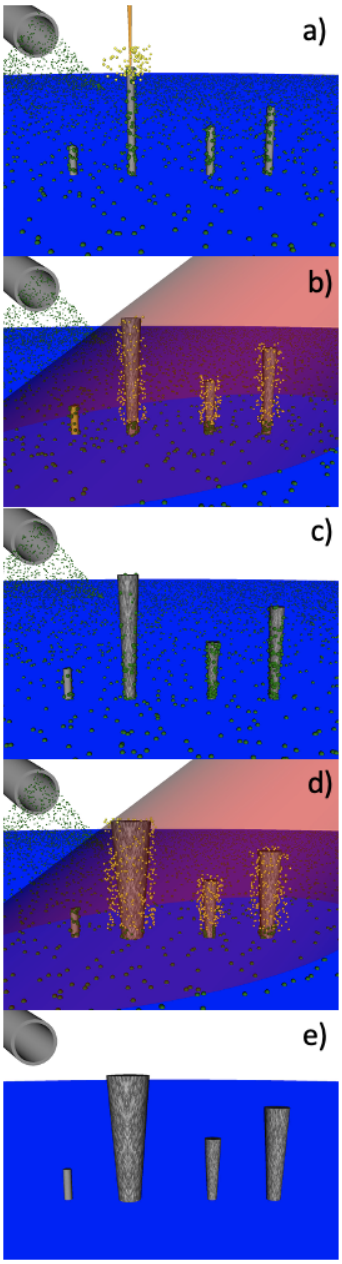

Figure 1: Schematic images of localized photothermal deposition of nanostructures. a) As-deposited PtC_x nanostructures formed by focused electron beam induced deposition from $MeCpPtMe_3$ (green spheres) forming $C_yH_z$by-products (yellow spheres) and a condensed nanopillar deposit (grey). In a general sense, FEBID follows the scheme $C_5H_4CH_3Pt(CH_3)_3$ (*g*) + *e*- ⟶ PtC_x(*s*) + C_yH_z (*g*). Subsequent pulsed laser selected area deposition illustrating various times during the growth during the b) and d) laser-on and the c) and e) laser-off time. During the laser-on, the pulsed laser selectively heats the deposited nanostructure and raises the nanostructure above the decomposition threshold of the precursor molecules and thus decomposes the molecules into a condensed deposit and C_yH_z by-products. This reaction can be approximated by the scheme $C_5H_4CH_3Pt(CH_3)_3$ (*g*) + $h\nu$ ⟶ PtC_x(*s*) + C_yH_z (*g*) where laser-induce PtC_x deposits selectively on the FEBID. During the laser-off time, the pillars are below the decomposition temperature and thus precursors adsorb and desorb on the deposit until the next laser pulse.

While other coating approaches are useful in "blanket" covering the 3D structures and substrates simultaneously, the laser induced photothermal CVD enables area selectivity and a unique regime where deposition occurs only on the FEBID nanostructures as dictated by their thermal transport and material properties. It should be noted that we utilized $MeCpPtMe_3$ *in-situ* both for FEBID and CVD as a matter of convenience to demonstrate the more generalized phenomenon. Again, it is anticipated that nanostructures grown via other techniques can also be selectively deposited and the laser CVD process should be ubiquitous to other precursors that do not photolytically decompose, so different materials/functionalities can be achieved with judicious choice of the 3D template and CVD precursors.

To test our hypothesis that the selected area deposition is governed by the thermal resistance of the nanostructure a series of FEBID nanopillars with various heights and similar diameters were deposited. The photothermal CVD process was documented via sequential SEM secondary electron (SE) imaging resulting in videos (Supporting video V1) that were analyzed frame-by-frame with a semi-automated, computer vision algorithm (Supporting information S2). To confirm the nanostructure evolution is not dominated by the electron beam exposure that occurs during imaging, exposures with and without video capture were taken and minimal difference was observed in these experiments. Additionally, deposition was attempted with and without the precursor gas flow to confirm the adventitious adsorbed carbon was not the precursor source and minimal changes were observed without platinum precursor flow.

To correlate the selected area deposition to nanostructure temperature, the measurements from the computer vision analysis of the evolving features were used as input to a COMSOL heat flow model derived from the absorbed laser energy and the nanostructure properties. The power input to the nanostructure for the simulation is estimated from fractional laser energy absorbed in the nanopillar $Q_{abs}=P_o \times (1-R) \times (1-e^{-A2r}) \times \frac{2rl}{\pi r_{laser}^2})$ where P_o is the total laser power, R is the reflectance $[(1-n_{PtCx})^2+k_{PtCx}^2]/[(1+n_{PtCx})^2+k_{PtCx}^2]$, A is the linear absorption or attenuation coefficient ($4\pi kPtC_x/\lambda$), l is the nanopillar length, r is the nanopillar radius, r_{laser} is the laser spot radius and λ is the laser wavelength. The optical constants n_{PtCx} and k_{PtCx} are the refractive index and extinction coefficient of the nanopillar template and were taken from previous literature to be 1.87 and 0.31, respectively, which was approximated by the Maxwell-Garnett effective medium approximation for PtC_5[68] and the heat capacity, and density were previously reported to be, 1250 kg/m^3, and 700 J/(kg-K), respectively[69]. The geometry of the nanopillar was simplified and assumed to be a cylindrical shape using an effective radius. To determine the

effective radius, we used our computer vision algorithm to measure the pillar radius every pixel, which for our typical image is on the order of 4 nm along the nanopillar length. We subsequently average the measured radii but exclude the top and bottom 20% of the as-growing structure. The thermal conductivity of the nanopillar was estimated to be 8.0 W/(m-K). It is important to note that the thermal conductivity was used as a tuning parameter to calibrate our simulations to the experimental observations. By simulating the pillar geometry and laser conditions at which the onset of laser CVD is observed we varied the thermal conductivity of the pillar material until our simulated peak nanopillar temperatures were approximately equal to the reported thermal decomposition temperature of the precursor (~ 600 K)[70]. The underlying assumption here is that the onset of laser CVD in our experiments occurs when the peak nanopillar temperature reaches this decomposition temperature, which ignores any potential catalytic effects of the nanostructure. Conveniently, the thermal conductivity of the nanopillar indicated by our tuning simulations is consistent with previous literature reports[71]. See Supporting information S3 for full sensitivity analysis of the thermal simulations.

The calculated absorbed power is then evenly distributed in the nanopillar volume which acts as the source term for the thermal model. COMSOL then discretizes or meshes the nanopillar and substrate and solves the heat transfer in the solid via finite element using the following equation:

$$\rho C_p \frac{\delta T}{\delta t} + \nabla q_{cond} = Q_{abs}$$

where q_{cond} is the heat flux by conduction (note we ignore radiation). The substrate is chosen to be deliberately large enough that we can set radial and lower z-dimensional constant temperature boundary conditions of 293 K without impacting peak temperatures at the nanopillar tip (see Supporting information S4). This results in temporal and spatial temperature information

in the nanopillars. As will be shown the peak temperature is located at the top of the nanopillar. Furthermore, the laser heating occurs rapidly on the order of 1-2 μs and then saturates. While the specific time of this saturation depends on the nanopillar geometry and properties, when we report the peak temperature, it is the temperature at the end of the pulse width and the top of the nanopillar.

In the plots that follow, the following procedure is used to generate the color-coded data which represents the modeled temperature. Scanning electron "videos" are collected in situ during the growth and at specific time increments the nanopillar length and effective radius are measured. Using the cylindrical approximation and the experimental laser parameters, the absorbed power is determined, and the cylinder is automatically constructed in COMSOL. The time dependent absorbed laser energy (integrated for power) is applied evenly to the cylinder and the full temporal and spatial temperature dependence of the nanopillar and substrate is determined. The peak temperature is determined for each time stamp and plotted as the heat map of the data. It is important to note that the modeling is semiquantitative and is intended to be illustrative. We interrogate several geometries (pillar height/diameters), and laser parameters such as power, pulse width, and frequencies. While some of the experiments show growth and modeled temperatures slightly below the threshold values and some exhibit growth initiation above the threshold values, we believe the preponderance of the data all point to a thermally driven CVD process as described in detail below..

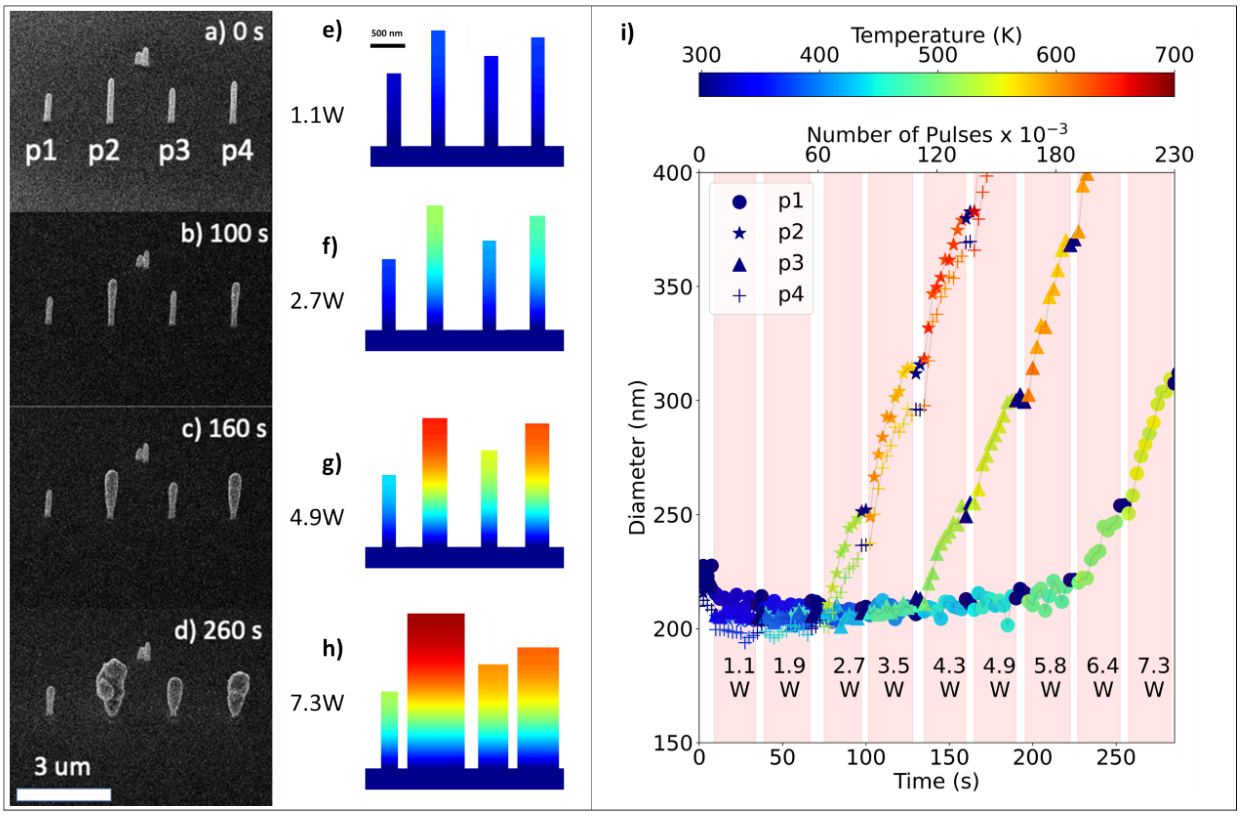

Figure 2: a) SEM images of as-deposited FEBID nanopillars of similar width grown to different heights and b)-d) selected area laser growth at various time stamps (the scale bar in d) applies to all SEM images). The laser growth conditions are 10 μs, 1000 Hz (0.01 duty cycle) where the laser power varies with time and can be inferred from the radius diameter versus time plot of the experiments shown in i). e-h) Corresponding maps of the modeled temperature of the 4 nanopillars at the end of a 10 μs laser pulse at the laser power listed in each panel. The modeled pillar geometry is constructed using cylindrical geometry approximations made from the neighboring SEM image. (note that the scale bar in e) applies to all of the modeled pillars in e-h)). i) Plot of nanopillar diameter as a function of total time (bottom axis) and laser pulse number (top axis). The laser power was systematically increased during the experiment where the highlighted regions list the applied laser power listed. The corresponding data point is color-

coded with temperature based on a COMSOL simulation of the geometry approximated from the captured SEM image at that time stamp.

During the experiment, the incident laser power was incrementally increased as indicated in Figure 2a until selected area deposition was evident on all nanopillars. The laser pulse duration (10 μs) and repetition rate (1000 Hz) were held constant for these experiments to probe the how power and geometry affected the growth. Figure 2b-e are SEM image captures at various times (see Supporting video V1 for the full experiment). To visualize the impact of the thermal resistance, the data points are colored coded with the simulated temperature where the evolving simulated temperature is based on the geometric data extracted via the computer vision algorithm, subsampling every 5 frames (see Supporting information S2 for details). The overarching trends illustrate that consistent with the higher thermal resistance ($l/K\pi r^2$), where K is the thermal conductivity, the taller nanopillars initiate photothermal CVD at lower laser power, whereas shorter nanopillars require higher power. Notably, all the nanopillars turn-on at similar simulated temperatures. The dark blue data points are zero laser power time intervals where the laser power was manually changed.

For long deposition durations, the experimental structures develop complex geometries. For instance, the large thermal mass of the substrate results in a low temperature boundary condition, which inhibits photothermal CVD near the base of the nanopillars. As a result, the nanostructures evolve from a cylinder to a more inverted conical shape as opposed to a conformal and isotropic cylinder. While we model the temperature during growth using a simplified cylindrical geometry, we acknowledge this deviation as a source of underestimating of the nanopillar temperature. Specifically, the low to zero growth at the pillar base will add a high series thermal

resistance. Our initial expectations were that as the nanopillars widened, the thermal resistance would decrease, the thermal mass would increase, and thus the nanopillar temperature would fall and yield lower photothermal CVD rates. However, simulations predict that some final structures are hotter than the initial as absorbance and the thermal series resistance at the base is operative. The expanding nanopillar suggests again that we are underestimating the nanostructure temperature due to the persistence of the thermal restriction at the base. Indeed, we observe experimentally that the long-exposure structures see phase-separation and what appears to be a flowing, molten phase (See Supporting video V2). Figure 2f) shows 3D rendered heat maps of our cylindrical approximation of the experimental geometries as extracted from the SEM image datasets in Figure 2d at the experimental optical power of 4.9 W. These simulations offer further insights into nanostructure evolution. Note the shortest nanopillar has the lowest temperature and is below the decomposition temperature and thus is not growing consistent with Figure 2a. The third nanopillar has experienced growth and the simulated temperature is comparable to the decomposition temperature. The second and fourth nanopillars are the hottest and have similar temperatures and have the steepest slopes consistent with higher growth rates. The top is hotter due to the quasi-1D heat transport confinement that occurs on the nanoscale. The tip stays above the decomposition temperature longer, thus deposition is preferred there. Inset next to each 3D nanopillar are time-temperature plots of the tip of the nanopillars. As demonstrated, the rise and fall time are on the order of 1 μs so the temperatures all saturate at the peak temperatures during each 10 μs pulses. More discussion on the validity of the thermal model and the time constant will be discussed below in the pulse width study.

To further explore the effect of geometry on the thermal resistance and initiation of the selected area deposition, several nanopillars of similar height were deposited with variable

diameters. Figure 3a illustrates the pillar diameter versus time (and number of pulses delivered) for the various nanopillar widths and 3b-c are the as-FEBID grown and post laser exposure SEM images, respectively. The laser power was again incrementally increased over time to note the onset of photothermal CVD. As is observed, the various diameters all initiate at the same laser power however, the nanopillars have slightly different simulated temperatures, where the smaller diameters are slightly higher than the larger diameters. Consistent with the higher temperatures, the diameter growth rates are higher for the narrower nanopillars. The fact that the growths all turn-on at the same power, does emphasize the point that while the thermal resistance increases with smaller diameter, the absorbed power below the absorption depth also decreases so the optical properties are also critical to the characteristic growth.

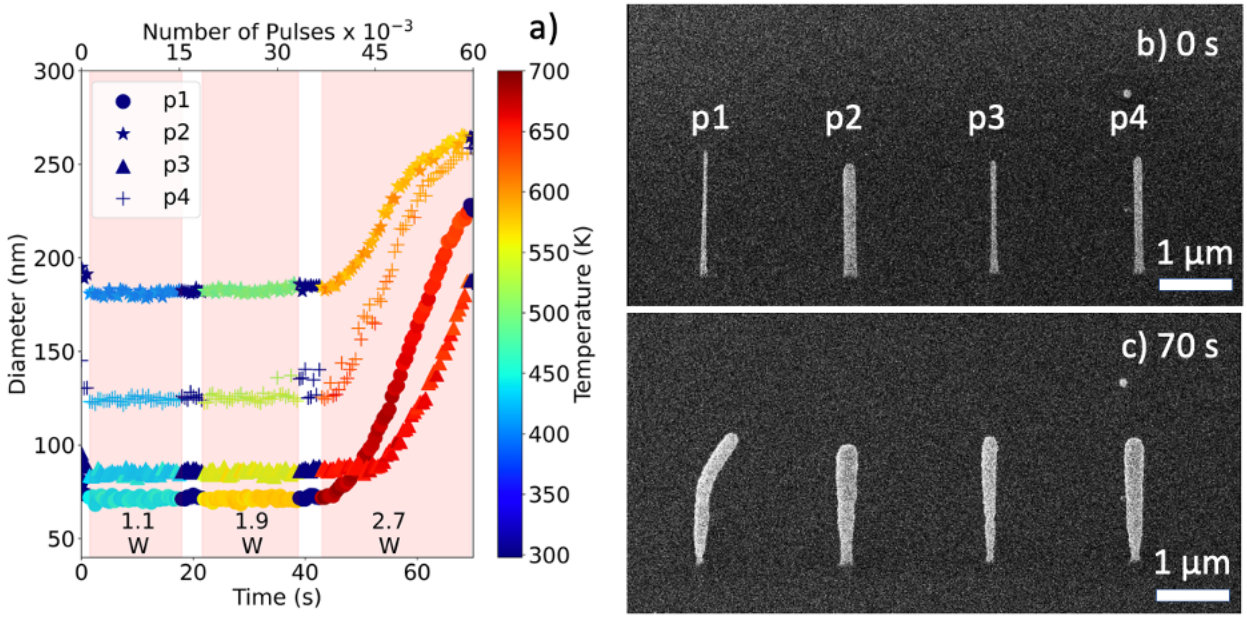

Figure 3. Plot of the a) nanopillar diameter as a function of time and number of laser pulses for nanopillars of similar initial height but variable initial diameter. SEM images of b) the as FEBID deposited and c) after selected area deposition.

From narrowest pillar in Figure 3, we estimate a per laser pulse diameter growth rate of ~ 8 pm/per pulse. See table 1 for summary of conditions and growth rates for experiments in Figures 3 and 4. Two possibilities for the selected area deposition mechanism are decomposition of precursor gas that is adsorbed during the laser-off time or decomposition of precursor gas molecules that arrive while the nanostructure is above a threshold decomposition temperature. To rationalize the deposition rate and test the proposed mechanisms, a series of photothermal CVD depositions were performed with constant laser pulse width (10 μs), on fixed geometry nanopillars and variable pulse repetition rate (250-5000 Hz). In this case, the lower repetition rate data has a longer inter-pulse delay time (ranging from 4000 to 250 μs, respectively). Figure 4 is the nanopillar diameter versus a) real time, b) number of pulses, and c) total laser on time (duty cycle x processing time). As illustrated, the rates (slopes) of the diameter versus pulse number is constant, which suggests that the deposition rate is constant. While at high repetition rate, the FEBID contribution during imaging is minimal, at lower frequency the laser duty cycle is sufficiently small that FEBID during imaging is non-negligible and affects the growth. Thus, there is some nanopillar broadening, which interestingly shortens the incubation number of pulses to initiate the growth. This again could be indicative of an absorption dominated initiation where the increasing nanopillar cross-sectional area increases the optical power absorption faster than the decrease in thermal resistance. Regardless of the incubation time, the near constant growth rate over the 20x change in frequency suggests the growth is dominated by the flux of $MeCpPtMe_3$ molecules that arrive at the nanostructure above a critical decomposition

temperature. Based on our previous estimate of the $MeCpPt^{IV}Me_3$ flux in our system ($1.8x10^3$ molecules/(nm^2-s)), we calculate a diameter per pulse (10 µs) growth rate of ~6 pm/pulse, which is in good agreement with the measured values. Deviations in the gas flux, and the thermal rise/decay time could both contribute to the differences in our model and experimentally observed per-pulse growth rates.

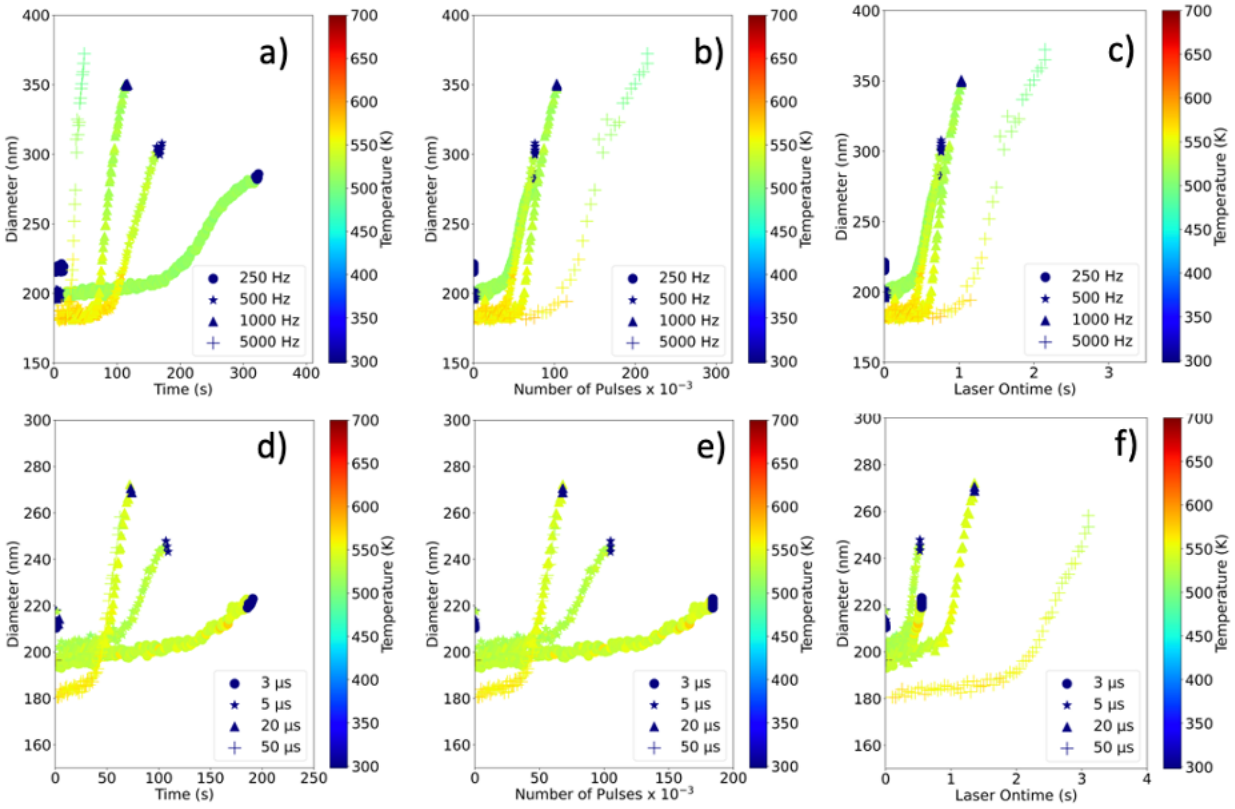

Figure 4. Plots of the diameter growth rate as a as a function of a) time, b) pulses and c) total laser on time processed at with various laser frequencies (noted in the figure legends). Plots of the diameter growth rate as a function of d) time and e) pulses and f) total laser on time processed at with various laser pulse widths (noted in the figure legend).

Finally, we investigate the effect that pulse width (3-50 μs) has on the growth rate, where we keep frequency (1000 Hz) and fixed nanopillar geometry constant. Figure 4 is the nanopillar diameter versus d) processing time, e) number of pulses, and f) total laser on-time (duty cycle x processing time). As shown in Supporting information S5, is important to note that at 10 μs pulse duration we are well within a steady-state thermal regime. Because the rise and fall time of the laser heating is on the order of 2 μs, thus the temperatures all saturate in this time scale.

We expect the nanostructure does not reach the precursor decomposition temperature with a pulse duration below ~2 μs, which has been confirmed experimentally (see 1 μs data in Supporting information S6). Thus, the laser exposure time is proportional to the pulse width and thus as illustrated in Figure 4e the per pulse growth rate is roughly proportional to the pulse width, except that the 20 and 50 μs data are similar. Figure 4f normalizes the data to total laser on-time. Interestingly, the initial incubation laser on-time to start growth is proportional to the effective initial diameter which scales with the pulse width. This diameter-dependence may again be indicating the importance of the optical absorption term in this length scale as larger initial cross-sectional areas decrease this incubation time. We speculate one cause could be a reordering of the nanostructure that is governed by the initial stages of laser irradiation where the as-FEBID deposited nanopillars densify proportional to the laser pulse width, and thus have slower initial growth. In future work, we will study in more detail the effects that the initial densification has on the growth process, including the density, optical, and thermal properties. Suffice it to say that there are subtle feedback processes involved in the early stages of the laser irradiation that affects the subsequent growth.

Summarily, the selected area laser CVD process is controlled by several variables. First of all, we show that the growth is consistent with a photothermal CVD process in which the high

temperatures are selectively achieved on the nanostructures relative to the substrate because of the combined optical and thermal properties of the nanoscale geometries. Because the growth only occurs when the structures exceed the threshold for the precursor dissociation, and because we are implementing a pulsed laser source, the laser power and duty cycle of the laser (pulse width and frequency) affects the growth rate normalized by the processing time. Finally, consistent with most thermal CVD processes, the growth rate is also dependent on the precursor flux. In our experiments constant precursor flux is maintained by: 1) consistent positioning of the processing region relative to the gas injection system; 2) constant precursor temperature; and 3) monitoring a constant chamber pressure.

Table 1. Summary of diameter growth rates at various experimental parameters.

Figure	Label	Laser Rate (Hz)	Pulse Width (μs)	Laser Power (W)	Deposition Rate (nm/s)	Deposition Rate (pm/pulse)
Fig 3	p3	1000	10	2.7	5.08	5.08
Fig 3	p2	1000	10	2.7	5.38	5.38
Fig 3	p4	1000	10	2.7	7.41	7.41
Fig 3	p1	1000	10	2.7	7.97	7.97
Fig 4 (a-c)	250 Hz	250	10	4.9	0.73	2.92
Fig 4 (a-c)	500 Hz	500	10	4.9	1.77	3.54
Fig 4 (a-c)	1000 Hz	1000	10	4.9	4.65	4.65
Fig 4 (a-c)	5000 Hz	5000	10	4.9	9.10	1.82
Fig 4 (d-f)	3 μs	1000	3	4.9	0.47	0.47
Fig 4 (d-f)	5 μs	1000	5	4.9	0.87	0.87
Fig 4 (d-f)	20 μs	1000	20	4.9	2.09	2.09
Fig 4 (d-f)	50 μs	1000	50	4.9	2.16	2.16

To elucidate the elemental distribution of the laser deposited structures, high-resolution EDS is presented in figure 5b. It can be seen by the EDS map that the bright crystallites in the SEM are platinum-rich and point spectra in these regions confirm the higher platinum concentration. However as seen in the cross-section of figure 5d, the platinum nanoparticles seem to migrate towards the surface, so the carbon-rich interior makes it difficult to determine the exact purity, due to the extended penetration of the electron beam.

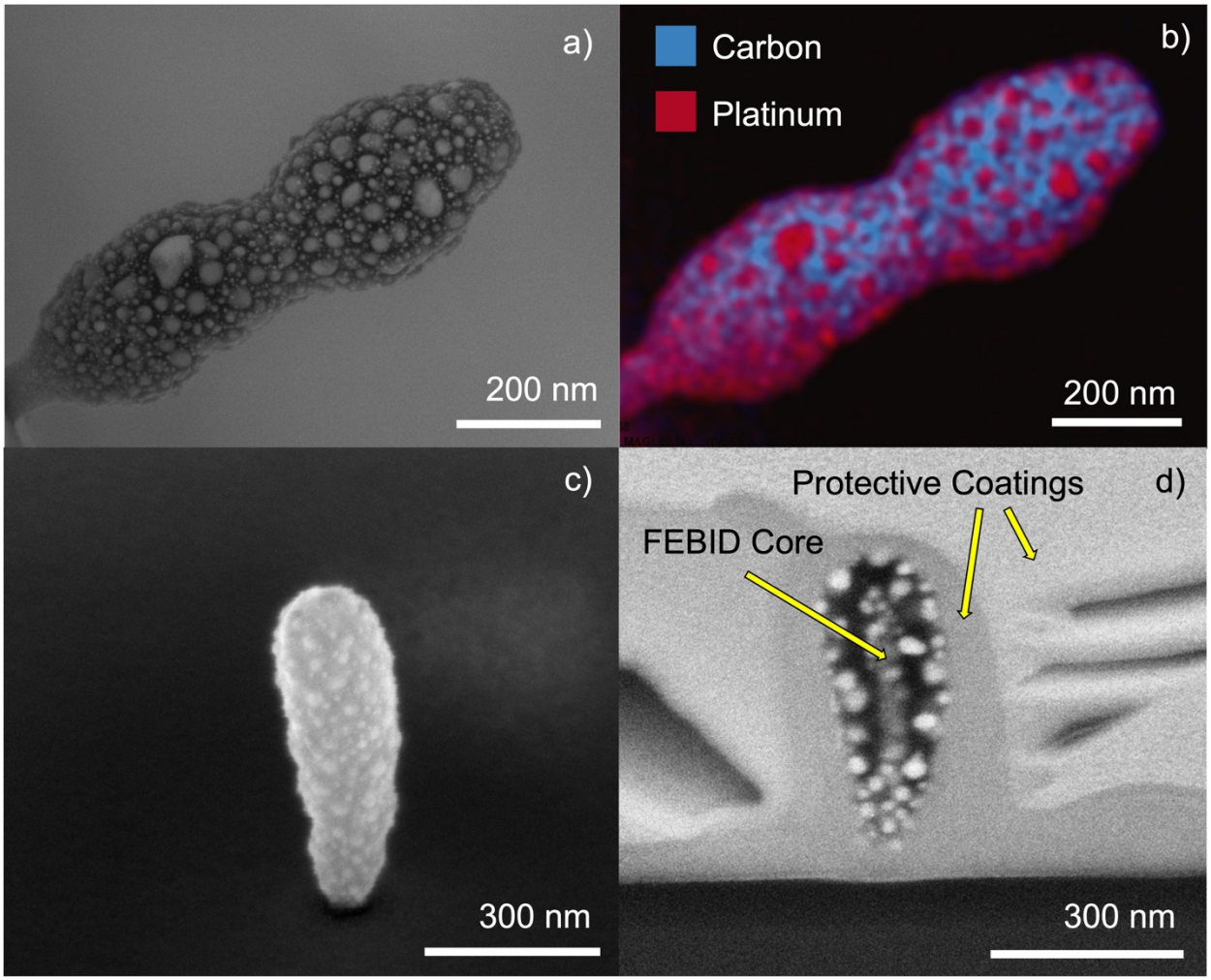

Figure 5. a) SEM image and b) EDS map of a of nanopillar after selected area laser processing. EDS maps of the pillar showing platinum-rich regions embedded in a C matrix indicating phase

separation and Pt grain growth during the laser processing. c) SEM image of an as laser grown pillar and the associated backscatter SEM image of a FIB cross-section showing the phase separation where Pt are the bright regions. The light, top amorphous material is a focused ion beam induced deposition protective layer for cross-sectioning, and the darker amorphous layer under that is initial FEBID protective deposition. The EBID as-deposited nanostructures were grown using a single pixel dwell at 5kV, 98 pA. 75nm beam diameter by defocusing, for 40s (a,b) and 30s (c,d) Laser CVD was accomplished using 4.8W, 10 μs 915 nm pulses at 1kHz for 60 s.

The phase separation and larger crystallites are not unexpected. Because of the limited solubility of Pt and C, the typical FEBID-grown material is a nanogranular composite of Pt grains in an amorphous carbon matrix. As several have observed, annealing or higher temperature growth of PtC_x deposits, results in coarsening of the Pt grains. Similar observations have been made in FeCO deposits[72] from the $Fe_2(CO)_9$ precursor, where initially homogeneous amorphous FeCO nanowire deposits were grown, in situ STEM characterization revealed phase separation and coarsening of Fe grains along the nanopillar axis. As discussed above, the $Co_2(CO)_8$ precursor results in much higher purity as-deposited FEBID Co nanowires up to ~ 70%[73]. They also showed that annealing these structures in vacuum up to 600^{o}C result in a purity on the order of 95% with a concomitant narrowing of the nanowire. The improved crystallinity and purity results in superior magnetic properties.

In Figure 6a, we demonstrate the ability to uniformly and selectively deposit on an array of simple FEBID structures in parallel with reasonable fidelity despite somewhat inhomogeneous laser irradiance in the field of view of the image (~ 20x20 μm). Additionally, Figure 6c

demonstrates a functionalized head-to-head 3d split ring resonator[18]; while Pt is not plasmonically active, selectively functionalizing these structures with gold using for instance the common FEBID gold acetylacetonate precursor could lead to plasmonically active 3D structures[18]. Future work will explore new precursors to realize magnetic ($Co_2(CO)_8$)[74], and plasmonic (Au precursors), as well as co-reactants such as oxygen and water to reduce the carbon content in the functional coatings.

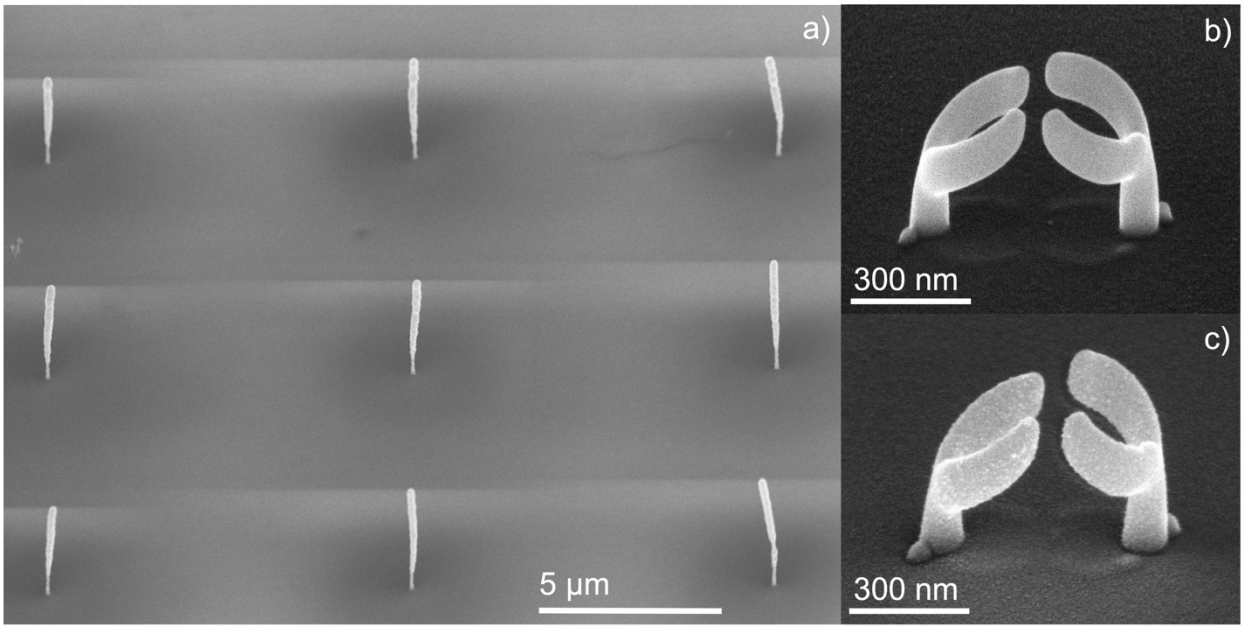

Figure 6. **a**) A 3x3 array of FEBID nanorods grown by FEBID depositions and coated in parallel via the selected area laser processing. Head-to-head comparison of a 3D coupled split ring resonator as FEBID grown **b**) and subsequently deposited with the selected area CVD **c**).

Experimental/Methods

All experiments were conducted in a dual beam FIB/SEM (FEI Nova 600) equipped with gas injection system (GIS) hardware for deposition of platinum and an in-situ pulsed laser system (Waviks Vesta) focused coincident to the electron beam at the eucentric position of the system. The laser source consists of 3 fiber-coupled laser diodes with wavelengths (915 nm, 785 nm, and 405 nm) delivering focused, unpolarized light with variable pulse duration (10 ns to continuous wave) with repetition rates ranging up to several MHz. Note the 20 W 915 nm laser is coupled to a multimode fiber with a ~ 100 μm diameter and the several hundred mW 785 nm and 405 nm laser diodes are coupled to a 5 μm diameter single mode fiber. All the experiments here used the 915 nm multimode fiber system. Positioning of GIS and the laser source on opposing sides of the chamber allows for simultaneous insertion of the laser source and GIS needle with both directed coincidentally to the eucentric position. This configuration is well suited for the required experiments due to the ability to tilt the stage between FEBID and laser CVD positions without losing focus/positioning of the SEM, laser, or GIS.

While we have demonstrated that this process is nearly substrate-independent, all systematic data presented here was performed a silicon substrate.

All work presented here was carried out using a 5 keV and 98 pA for FEBID growth and in situ imaging. The nanopillar height is controlled by adjusting the beam current density and exposure time. The nanopillar diameter can be intentionally increased by applying a defocus to increase the beam diameter (which also reduces the current density) for a single pixel dwell or by patterning multiple pixels in an area scan. The GIS is inserted while the stage is at 0^{o} tilt at the eucentric height, the GIS valve is opened and allowed to stabilize for a several minutes, and the patterning of single or arrays of FEBID nanopillars is initiated such that nanopillars grow normal

to the plane of the sample. In the case of 5kV, 98pA growth conditions, in-focus depositions result in nanopillar diameters on the order of 50 nm.

Following FEBID nanostructure growth, the GIS is closed, retracted, and the stage is tilted to 52°. At this point, the GIS is reinserted, gas flow re-established, and laser irradiation is initiated with the desired wavelength, power, pulse duration, and repetition rate for the specified duration of the laser CVD process. We have demonstrated little variation in the laser CVD process as a function of incidence angle, so 52° is chosen as a matter of convenience as it allows for SEM imaging of the growing nanostructure during laser irradiation. This enables us to collect time-series data and monitor the growth kinetics of the process. It is important to note that while we are imaging with the SEM during laser CVD, we are continually decomposing the precursor over the field of view via FEBID. At sufficiently high laser duty cycles (product of the pulse width and pulse frequency), where the laser induced growth rates are high, the FEBID contributions are minimal, but as shown in Supporting Information S6 , lower laser duty cycle (slower laser growth) can lead to discernible FEBID contributions .

Measurement of the evolving nanostructures through the hundreds of time-series images is accomplished via an automated computer vision and image processing algorithm. Details of this method are discussed in Supporting information S2.

Conclusions

We have demonstrated an *in-situ* selected area photothermal CVD process that can be used to controllably deposit onto complex 3D nanoarchitectures in parallel due to their unique thermal transport properties. The 3D nanostructures were grown via FEBID and subsequently photothermally deposited using the $MeCpPt^{IV}Me_3$ precursor. Again, it is anticipated that nanostructures grown via other techniques can also be selectively deposited and the laser CVD

process should be ubiquitous to other precursors that do not photolytically decompose, thus, by judicious choice of precursor, the laser CVD process can be used to selectively coat the 3D nanostructures and thus functionalize them with a targeted property. Various initial nanopillar geometries were grown and simulations reveal that the unique thermal transport properties of the nanostructures enable the selected area growth. By tuning the thermal conductivity simulations were initially tuned with a fixed geometry to the known precursor decomposition temperature. Subsequent experiments of various nanopillar geometries, laser frequency and pulse widths reveal excellent agreement in the simulated growth temperatures. The experiments suggest the growth mechanism is due to the decomposition of the flux of precursor gas molecules that strike the nanostructure when the nanostructure exceeds the decomposition temperature. Thus, the diameter growth rate is proportional to the cumulative laser on-time, thus higher laser frequency and higher pulse widths lead to faster growth.

Supporting Information

Additional information showing deposition on a variety of substrates, computer-vision details, geometry and parameter effects on thermal modeling, steady-state heating pulse width effects then corresponding 1μs experimental data. SEM videos of Figure 2 deposition; liquid, molten material flow.

Acknowledgments

This research was supported by the Center for Nanophase Materials Sciences, which is a U.S. Department of Energy Office of Science user facility at Oak Ridge National Laboratory (ORNL) Support for SJR was partially provided through Strategic Hire funding through the Laboratory

Directed Research and Development Program of Oak Ridge National Laboratory, managed by UT-Battelle, LLC, for the U. S. Department of Energy.

References

(1) Córdoba, R. Editorial for the Special Issue on Nanofabrication with Focused Electron/Ion Beam Induced Processing. *Micromachines* **2021**, *12* (8), 893. https://doi.org/10.3390/mi12080893.

(2) Huth, M.; Porrati, F.; Dobrovolskiy, O. V. Focused Electron Beam Induced Deposition Meets Materials Science. *Microelectron. Eng.* **2018**, *185–186*, 9–28. https://doi.org/10.1016/j.mee.2017.10.012.

(3) Lewis, J. A.; Smay, J. E.; Stuecker, J.; Cesarano, J. Direct Ink Writing of Three-Dimensional Ceramic Structures. *J. Am. Ceram. Soc.* **2006**, *89* (12), 3599–3609. https://doi.org/10.1111/j.1551-2916.2006.01382.x.

(4) Lewis, J. A. Direct Ink Writing of 3D Functional Materials. *Adv. Funct. Mater.* **2006**, *16* (17), 2193–2204. https://doi.org/10.1002/adfm.200600434.

(5) Jeon, H.; Schmidt, R.; Barton, J. E.; Hwang, D. J.; Gamble, L. J.; Castner, D. G.; Grigoropoulos, C. P.; Healy, K. E. Chemical Patterning of Ultrathin Polymer Films by Direct-Write Multiphoton Lithography. *J. Am. Chem. Soc.* **2011**, *133* (16), 6138–6141. https://doi.org/10.1021/ja200313q.

(6) Malinauskas, M.; Danilevičius, P.; Juodkazis, S. Three-Dimensional Micro-/Nano-Structuring via Direct Write Polymerization with Picosecond Laser Pulses. *Opt. Express* **2011**, *19* (6), 5602–5610. https://doi.org/10.1364/OE.19.005602.

(7) Zhang, B.; He, J.; Li, X.; Xu, F.; Li, D. Micro/Nanoscale Electrohydrodynamic Printing: From 2D to 3D. *Nanoscale* **2016**, *8* (34), 15376–15388. https://doi.org/10.1039/C6NR04106J.

(8) Piner, R. D.; Zhu, J.; Xu, F.; Hong, S.; Mirkin, C. A. "Dip-Pen" Nanolithography. *Science* **1999**. https://doi.org/10.1126/science.283.5402.661.

(9) Osgood, R. M. Laser Microchemistry and Its Application to Electron-Device Fabrication. *Annu. Rev. Phys. Chem.* **1983**, *34* (1), 77–101. https://doi.org/10.1146/annurev.pc.34.100183.000453.

(10) Ehrlich, D. J.; Tsao, J. Y. Chapter 3 - Laser Direct Writing for VLSI* *This Work Was Supported by the Defense Advanced Research Projects Agency, the Department of the Air Force (in Part under a Specific Program Sponsored by the Air Force Office of Scientific Research), and the Army Research Office. In *VLSI Electronics Microstructure Science*; Einspruch, N. G., Ed.; Elsevier, 1983; Vol. 7, pp 129–164. https://doi.org/10.1016/B978-0-12-234107-6.50008-9.

(11) Bert Huis in 't Veld; Overmeyer, L.; Schmidt, M.; Wegener, K.; Malshe, A.; Bartolo, P. Micro Additive Manufacturing Using Ultra Short Laser Pulses. *CIRP Ann.* **2015**, *64* (2), 701–724. https://doi.org/10.1016/j.cirp.2015.05.007.

(12) Piqué, A.; Auyeung, R. C. Y.; Kim, H.; Charipar, N. A.; Mathews, S. A. Laser 3D Micro-Manufacturing. *J. Phys. Appl. Phys.* **2016**, *49* (22), 223001. https://doi.org/10.1088/0022-3727/49/22/223001.
(13) Hirt, L.; Reiser, A.; Spolenak, R.; Zambelli, T. Additive Manufacturing of Metal Structures at the Micrometer Scale. *Adv. Mater.* **2017**, *29* (17), 1604211. https://doi.org/10.1002/adma.201604211.
(14) Gruber, G.; Urgell, C.; Tavernarakis, A.; Stavrinadis, A.; Tepsic, S.; Magén, C.; Sangiao, S.; de Teresa, J. M.; Verlot, P.; Bachtold, A. Mass Sensing for the Advanced Fabrication of Nanomechanical Resonators. *Nano Lett.* **2019**, *19* (10), 6987–6992. https://doi.org/10.1021/acs.nanolett.9b02351.
(15) Lukashenko, S. Y.; Mukhin, I. S.; Komissarenko, F. E.; Gorbenko, O. M.; Sapozhnikov, I. D.; Felshtyn, M. L.; Uskov, A. V.; Golubok, A. O. Resonant Mass Detector Based on Carbon Nanowhiskers with Traps for Nanoobjects Weighing. *Phys. Status Solidi A* **2018**, *215* (21), 1800046. https://doi.org/10.1002/pssa.201800046.
(16) Plank, H.; Winkler, R.; Schwalb, C. H.; Hütner, J.; Fowlkes, J. D.; Rack, P. D.; Utke, I.; Huth, M. Focused Electron Beam-Based 3D Nanoprinting for Scanning Probe Microscopy: A Review. *Micromachines* **2020**, *11* (1), 48. https://doi.org/10.3390/mi11010048.
(17) Wu, W.; Pauly, M. Chiral Plasmonic Nanostructures: Recent Advances in Their Synthesis and Applications. *Mater. Adv.* **2022**, *3* (1), 186–215. https://doi.org/10.1039/D1MA00915J.
(18) Pakeltis, G.; Hu, Z.; Nixon, A. G.; Mutunga, E.; Anyanwu, C. P.; West, C. A.; Idrobo, J. C.; Plank, H.; Masiello, D. J.; Fowlkes, J. D.; Rack, P. D. Focused Electron Beam Induced Deposition Synthesis of 3D Photonic and Magnetic Nanoresonators. *ACS Appl. Nano Mater.* **2019**, *2* (12), 8075–8082. https://doi.org/10.1021/acsanm.9b02182.
(19) Keller, L.; Al Mamoori, M. K. I.; Pieper, J.; Gspan, C.; Stockem, I.; Schröder, C.; Barth, S.; Winkler, R.; Plank, H.; Pohlit, M.; Müller, J.; Huth, M. Direct-Write of Free-Form Building Blocks for Artificial Magnetic 3D Lattices. *Sci. Rep.* **2018**, *8* (1), 6160. https://doi.org/10.1038/s41598-018-24431-x.
(20) Fowlkes, J. D.; Winkler, R.; Lewis, B. B.; Stanford, M. G.; Plank, H.; Rack, P. D. Simulation-Guided 3D Nanomanufacturing via Focused Electron Beam Induced Deposition. *ACS Nano* **2016**, *10* (6), 6163–6172. https://doi.org/10.1021/acsnano.6b02108.
(21) Smith, D. A.; Fowlkes, J. D.; Rack, P. D. A Nanoscale Three-Dimensional Monte Carlo Simulation of Electron-Beam-Induced Deposition with Gas Dynamics. *Nanotechnology* **2007**, *18* (26), 265308. https://doi.org/10.1088/0957-4484/18/26/265308.
(22) Smith, D. A.; Fowlkes, J. D.; Rack, P. D. Simulating the Effects of Surface Diffusion on Electron Beam Induced Deposition via a Three-Dimensional Monte Carlo Simulation. *Nanotechnology* **2008**, *19* (41), 415704. https://doi.org/10.1088/0957-4484/19/41/415704.
(23) Smith, D. A.; Fowlkes, J. D.; Rack, P. D. Understanding the Kinetics and Nanoscale Morphology of Electron-Beam-Induced Deposition via a Three-Dimensional Monte Carlo Simulation: The Effects of the Precursor Molecule and the Deposited Material. *Small* **2008**, *4* (9), 1382–1389. https://doi.org/10.1002/smll.200701133.
(24) Cullen, J.; Lobo, C. J.; Ford, M. J.; Toth, M. Electron-Beam-Induced Deposition as a Technique for Analysis of Precursor Molecule Diffusion Barriers and Prefactors. *ACS Appl. Mater. Interfaces* **2015**, *7* (38), 21408–21415. https://doi.org/10.1021/acsami.5b06341.
(25) Salvat-Pujol, F.; Valentí, R.; Werner, W. S. Surface Excitations in the Modelling of Electron Transport for Electron-Beam-Induced Deposition Experiments. *Beilstein J. Nanotechnol.* **2015**, *6* (1), 1260–1267. https://doi.org/10.3762/bjnano.6.129.

(26) Fowlkes, J. D.; Winkler, R.; Mutunga, E.; Rack, P. D.; Plank, H. Simulation Informed CAD for 3D Nanoprinting. *Micromachines* **2020**, *11* (1), 8. https://doi.org/10.3390/mi11010008.
(27) Fowlkes, J. D.; Winkler, R.; Lewis, B. B.; Fernández-Pacheco, A.; Skoric, L.; Sanz-Hernández, D.; Stanford, M. G.; Mutunga, E.; Rack, P. D.; Plank, H. High-Fidelity 3D-Nanoprinting via Focused Electron Beams: Computer-Aided Design (3BID). *ACS Appl. Nano Mater.* **2018**, *1* (3), 1028–1041. https://doi.org/10.1021/acsanm.7b00342.
(28) Keller, L.; Huth, M. Pattern Generation for Direct-Write Three-Dimensional Nanoscale Structures via Focused Electron Beam Induced Deposition. *Beilstein J. Nanotechnol.* **2018**, *9*, 2581–2598. https://doi.org/10.3762/bjnano.9.240.
(29) Botman, A.; Mulders, J. J. L.; Weemaes, R.; Mentink, S. Purification of Platinum and Gold Structures after Electron-Beam-Induced Deposition. *Nanotechnology* **2006**, *17* (15), 3779–3785. https://doi.org/10.1088/0957-4484/17/15/028.
(30) Barth, S.; Huth, M.; Jungwirth, F. Precursors for Direct-Write Nanofabrication with Electrons. *J. Mater. Chem. C* **2020**, *8* (45), 15884–15919. https://doi.org/10.1039/D0TC03689G.
(31) Winkler, R.; Geier, B.; Plank, H. Spatial Chemistry Evolution during Focused Electron Beam-Induced Deposition: Origins and Workarounds. *Appl. Phys. A* **2014**, *117* (4), 1675–1688. https://doi.org/10.1007/s00339-014-8496-y.
(32) Makise, K.; Mitsuishi, K.; Shimojo, M.; Shinozaki, B. Microstructural Analysis and Transport Properties of MoO and MoC Nanostructures Prepared by Focused Electron Beam-Induced Deposition. *Sci. Rep.* **2014**, *4* (1), 5740. https://doi.org/10.1038/srep05740.
(33) Weber, M.; Koops, H. W. P.; Rudolph, M.; Kretz, J.; Schmidt, G. New Compound Quantum Dot Materials Produced by Electron-beam Induced Deposition. *J. Vac. Sci. Technol. B Microelectron. Nanometer Struct. Process. Meas. Phenom.* **1995**, *13* (3), 1364–1368. https://doi.org/10.1116/1.587854.
(34) Sengupta, S.; Li, C.; Baumier, C.; Kasumov, A.; Guéron, S.; Bouchiat, H.; Fortuna, F. Superconducting Nanowires by Electron-Beam-Induced Deposition. *Appl. Phys. Lett.* **2015**, *106* (4), 042601. https://doi.org/10.1063/1.4906269.
(35) Mulders, J. J. L.; Belova, L. M.; Riazanova, A. Electron Beam Induced Deposition at Elevated Temperatures: Compositional Changes and Purity Improvement. *Nanotechnology* **2010**, *22* (5), 055302. https://doi.org/10.1088/0957-4484/22/5/055302.
(36) Porrati, F.; Sachser, R.; Huth, M. The Transient Electrical Conductivity of W-Based Electron-Beam-Induced Deposits during Growth, Irradiation and Exposure to Air. *Nanotechnology* **2009**, *20* (19), 195301. https://doi.org/10.1088/0957-4484/20/19/195301.
(37) Gavagnin, M.; Wanzenboeck, H. D.; Belic, D.; Shawrav, M. M.; Persson, A.; Gunnarsson, K.; Svedlindh, P.; Bertagnolli, E. Magnetic Force Microscopy Study of Shape Engineered FEBID Iron Nanostructures. *Phys. Status Solidi A* **2014**, *211* (2), 368–374. https://doi.org/10.1002/pssa.201330114.
(38) Gavagnin, M.; Wanzenboeck, H. D.; Belić, D.; Bertagnolli, E. Synthesis of Individually Tuned Nanomagnets for Nanomagnet Logic by Direct Write Focused Electron Beam Induced Deposition. *ACS Nano* **2013**, *7* (1), 777–784. https://doi.org/10.1021/nn305079a.
(39) Lukasczyk, T.; Schirmer, M.; Steinrück, H.-P.; Marbach, H. Electron-Beam-Induced Deposition in Ultrahigh Vacuum: Lithographic Fabrication of Clean Iron Nanostructures. *Small* **2008**, *4* (6), 841–846. https://doi.org/10.1002/smll.200701095.

(40) Córdoba, R.; Sharma, N.; Kölling, S.; Koenraad, P. M.; Koopmans, B. High-Purity 3D Nano-Objects Grown by Focused-Electron-Beam Induced Deposition. *Nanotechnology* **2016**, *27* (35), 355301. https://doi.org/10.1088/0957-4484/27/35/355301.
(41) Rodríguez, L. A.; Deen, L.; Córdoba, R.; Magén, C.; Snoeck, E.; Koopmans, B.; Teresa, J. M. D. Influence of the Shape and Surface Oxidation in the Magnetization Reversal of Thin Iron Nanowires Grown by Focused Electron Beam Induced Deposition. *Beilstein J. Nanotechnol.* **2015**, *6* (1), 1319–1331. https://doi.org/10.3762/bjnano.6.136.
(42) Utke, I.; Friedli, V.; Michler, J.; Bret, T.; Multone, X.; Hoffmann, P. Density Determination of Focused-Electron-Beam-Induced Deposits with Simple Cantilever-Based Method. *Appl. Phys. Lett.* **2006**, *88* (3), 031906. https://doi.org/10.1063/1.2158516.
(43) Utke, I.; Bret, T.; Laub, D.; Buffat, Ph.; Scandella, L.; Hoffmann, P. Thermal Effects during Focused Electron Beam Induced Deposition of Nanocomposite Magnetic-Cobalt-Containing Tips. *Microelectron. Eng.* **2004**, *73–74*, 553–558. https://doi.org/10.1016/j.mee.2004.02.084.
(44) Nikulina, E.; Idigoras, O.; Vavassori, P.; Chuvilin, A.; Berger, A. Magneto-Optical Magnetometry of Individual 30 Nm Cobalt Nanowires Grown by Electron Beam Induced Deposition. *Appl. Phys. Lett.* **2012**, *100* (14), 142401. https://doi.org/10.1063/1.3701153.
(45) Ehrichs, E. E.; Smith, W. F.; de Lozanne, A. L. Four-Probe Resistance Measurements of Nickel Wires Written with a Scanning Tunneling Microscope/Scanning Electron Microscope System. *Ultramicroscopy* **1992**, *42–44*, 1438–1442. https://doi.org/10.1016/0304-3991(92)90462-S.
(46) Warneke, Z.; Rohdenburg, M.; Warneke, J.; Kopyra, J.; Swiderek, P. Electron-Driven and Thermal Chemistry during Water-Assisted Purification of Platinum Nanomaterials Generated by Electron Beam Induced Deposition. *Beilstein J. Nanotechnol.* **2018**, *9*, 77–90. https://doi.org/10.3762/bjnano.9.10.
(47) Wnuk, J. D.; Gorham, J. M.; Rosenberg, S. G.; van Dorp, W. F.; Madey, T. E.; Hagen, C. W.; Fairbrother, D. H. Electron Induced Surface Reactions of the Organometallic Precursor Trimethyl(Methylcyclopentadienyl)Platinum(IV). *J. Phys. Chem. C* **2009**, *113* (6), 2487–2496. https://doi.org/10.1021/jp807824c.
(48) Sachser, R.; Porrati, F.; Schwalb, C. H.; Huth, M. Universal Conductance Correction in a Tunable Strongly Coupled Nanogranular Metal. *Phys. Rev. Lett.* **2011**, *107* (20), 206803. https://doi.org/10.1103/PhysRevLett.107.206803.
(49) Porrati, F.; Sachser, R.; Schwalb, C. H.; Frangakis, A. S.; Huth, M. Tuning the Electrical Conductivity of Pt-Containing Granular Metals by Postgrowth Electron Irradiation. *J. Appl. Phys.* **2011**, *109* (6), 063715. https://doi.org/10.1063/1.3559773.
(50) Plank, H.; Noh, J. H.; Fowlkes, J. D.; Lester, K.; Lewis, B. B.; Rack, P. D. Electron-Beam-Assisted Oxygen Purification at Low Temperatures for Electron-Beam-Induced Pt Deposits: Towards Pure and High-Fidelity Nanostructures. *ACS Appl. Mater. Interfaces* **2014**, *6* (2), 1018–1024. https://doi.org/10.1021/am4045458.
(51) Belić, D.; Shawrav, M. M.; Gavagnin, M.; Stöger-Pollach, M.; Wanzenboeck, H. D.; Bertagnolli, E. Direct-Write Deposition and Focused-Electron-Beam-Induced Purification of Gold Nanostructures. *ACS Appl. Mater. Interfaces* **2015**, *7* (4), 2467–2479. https://doi.org/10.1021/am507327y.
(52) Botman, A.; Mulders, J. J. L.; Hagen, C. W. Creating Pure Nanostructures from Electron-Beam-Induced Deposition Using Purification Techniques: A Technology Perspective. *Nanotechnology* **2009**, *20* (37), 372001. https://doi.org/10.1088/0957-4484/20/37/372001.

(53) Lewis, B. B.; Stanford, M. G.; Fowlkes, J. D.; Lester, K.; Plank, H.; Rack, P. D. Electron-Stimulated Purification of Platinum Nanostructures Grown via Focused Electron Beam Induced Deposition. *Beilstein J. Nanotechnol.* **2015**, *6*. https://doi.org/10.3762/bjnano.6.94.
(54) Mehendale, S.; Mulders, J. J. L.; Trompenaars, P. H. F. A New Sequential EBID Process for the Creation of Pure Pt Structures from MeCpPtMe3. *Nanotechnology* **2013**, *24* (14), 145303. https://doi.org/10.1088/0957-4484/24/14/145303.
(55) Geier, B.; Gspan, C.; Winkler, R.; Schmied, R.; Fowlkes, J. D.; Fitzek, H.; Rauch, S.; Rattenberger, J.; Rack, P. D.; Plank, H. Rapid and Highly Compact Purification for Focused Electron Beam Induced Deposits: A Low Temperature Approach Using Electron Stimulated H2O Reactions. *J. Phys. Chem. C* **2014**, *118* (25), 14009–14016. https://doi.org/10.1021/jp503442b.
(56) Noh, J. H.; Stanford, M. G.; Lewis, B. B.; Fowlkes, J. D.; Plank, H.; Rack, P. D. Nanoscale Electron Beam-Induced Deposition and Purification of Ruthenium for Extreme Ultraviolet Lithography Mask Repair. *Appl. Phys. A* **2014**, *117* (4), 1705–1713. https://doi.org/10.1007/s00339-014-8745-0.
(57) Fowlkes, J. D.; Geier, B.; Lewis, B. B.; Rack, P. D.; Stanford, M. G.; Winkler, R.; Plank, H. Electron Nanoprobe Induced Oxidation: A Simulation of Direct-Write Purification. *Phys. Chem. Chem. Phys.* **2015**, *17* (28), 18294–18304. https://doi.org/10.1039/C5CP01196E.
(58) Botman, A.; Hesselberth, M.; Mulders, J. J. L. Improving the Conductivity of Platinum-Containing Nano-Structures Created by Electron-Beam-Induced Deposition. *Microelectron. Eng.* **2008**, *85* (5), 1139–1142. https://doi.org/10.1016/j.mee.2007.12.036.
(59) Fang, J.-Y.; Qin, S.-Q.; Zhang, X.-A.; Liu, D.-Q.; Chang, S.-L. Annealing Effect of Platinum-Incorporated Nanowires Created by Focused Ion/Electron-Beam-Induced Deposition. *Chin. Phys. B* **2014**, *23* (8), 088111. https://doi.org/10.1088/1674-1056/23/8/088111.
(60) Gopal, V.; Radmilovic, V. R.; Daraio, C.; Jin, S.; Yang, P.; Stach, E. A. Rapid Prototyping of Site-Specific Nanocontacts by Electron and Ion Beam Assisted Direct-Write Nanolithography. *Nano Lett.* **2004**, *4* (11), 2059–2063. https://doi.org/10.1021/nl0492133.
(61) Langford, R. M.; Wang, T.-X.; Ozkaya, D. Reducing the Resistivity of Electron and Ion Beam Assisted Deposited Pt. *Microelectron. Eng.* **2007**, *84* (5), 784–788. https://doi.org/10.1016/j.mee.2007.01.055.
(62) Roberts, N. A.; Fowlkes, J. D.; Magel, G. A.; Rack, P. D. Enhanced Material Purity and Resolution via Synchronized Laser Assisted Electron Beam Induced Deposition of Platinum. *Nanoscale* **2012**, *5* (1), 408–415. https://doi.org/10.1039/C2NR33014H.
(63) Stanford, M. G.; Lewis, B. B.; Noh, J. H.; Fowlkes, J. D.; Rack, P. D. Inert Gas Enhanced Laser-Assisted Purification of Platinum Electron-Beam-Induced Deposits. *ACS Appl. Mater. Interfaces* **2015**, *7* (35), 19579–19588. https://doi.org/10.1021/acsami.5b02488.
(64) Utke, I.; Bret, T.; Laub, D.; Buffat, Ph.; Scandella, L.; Hoffmann, P. Thermal Effects during Focused Electron Beam Induced Deposition of Nanocomposite Magnetic-Cobalt-Containing Tips. *Microelectron. Eng.* **2004**, *73–74*, 553–558. https://doi.org/10.1016/j.mee.2004.02.084.
(65) Randolph, S. J.; Fowlkes, J. D.; Rack, P. D. Effects of Heat Generation during Electron-Beam-Induced Deposition of Nanostructures. *J. Appl. Phys.* **2005**, *97* (12), 124312. https://doi.org/10.1063/1.1942627.

(66) Mutunga, E.; Winkler, R.; Sattelkow, J.; Rack, P. D.; Plank, H.; Fowlkes, J. D. Impact of Electron-Beam Heating during 3D Nanoprinting. *ACS Nano* **2019**, *13* (5), 5198–5213. https://doi.org/10.1021/acsnano.8b09341.
(67) Winkler, R.; Lewis, B. B.; Fowlkes, J. D.; Rack, P. D.; Plank, H. High-Fidelity 3D-Nanoprinting via Focused Electron Beams: Growth Fundamentals. *ACS Appl. Nano Mater.* **2018**, *1* (3), 1014–1027. https://doi.org/10.1021/acsanm.8b00158.
(68) Stanford, M. G.; Lewis, B. B.; Noh, J. H.; Fowlkes, J. D.; Roberts, N. A.; Plank, H.; Rack, P. D. Purification of Nanoscale Electron-Beam-Induced Platinum Deposits via a Pulsed Laser-Induced Oxidation Reaction. *ACS Appl. Mater. Interfaces* **2014**, *6* (23), 21256–21263. https://doi.org/10.1021/am506246z.
(69) Mutunga, E.; Winkler, R.; Sattelkow, J.; Rack, P. D.; Plank, H.; Fowlkes, J. D. Impact of Electron-Beam Heating during 3D Nanoprinting. *ACS Nano* **2019**, *13* (5), 5198–5213. https://doi.org/10.1021/acsnano.8b09341.
(70) Faust, M.; Enders, M.; Bruns, M.; Bräse, S.; Gao, K.; Seipenbusch, M. Synthesis of Nanostructured Pt/Oxide Catalyst Particles by MOCVD Process at Ambient Pressure. *Surf. Coat. Technol.* **2013**, *230*, 284–289. https://doi.org/10.1016/j.surfcoat.2013.06.088.
(71) Lewis, B. B.; Winkler, R.; Sang, X.; Pudasaini, P. R.; Stanford, M. G.; Plank, H.; Unocic, R. R.; Fowlkes, J. D.; Rack, P. D. 3D Nanoprinting via Laser-Assisted Electron Beam Induced Deposition: Growth Kinetics, Enhanced Purity, and Electrical Resistivity. *Beilstein J. Nanotechnol.* **2017**, *8*, 801–812. https://doi.org/10.3762/bjnano.8.83.
(72) Pablo-Navarro, J.; Winkler, R.; Haberfehlner, G.; Magén, C.; Plank, H.; De Teresa, J. M. In Situ Real-Time Annealing of Ultrathin Vertical Fe Nanowires Grown by Focused Electron Beam Induced Deposition. *Acta Mater.* **2019**, *174*, 379–386. https://doi.org/10.1016/j.actamat.2019.05.035.
(73) Pablo-Navarro, J.; Magén, C.; de Teresa, J. M. Purified and Crystalline Three-Dimensional Electron-Beam-Induced Deposits: The Successful Case of Cobalt for High-Performance Magnetic Nanowires. *ACS Appl. Nano Mater.* **2018**, *1* (1), 38–46. https://doi.org/10.1021/acsanm.7b00016.
(74) Fernández-Pacheco, A.; Teresa, J. M. D.; Córdoba, R.; Ibarra, M. R. Magnetotransport Properties of High-Quality Cobalt Nanowires Grown by Focused-Electron-Beam-Induced Deposition. *J. Phys. Appl. Phys.* **2009**, *42* (5), 055005. https://doi.org/10.1088/0022-3727/42/5/055005.